An Improved Algorithm for Drift Diffusion Transport and Its Application on Large Scale Parallel Simulation of Resistive Random Access Memory Arrays

DA-WEI WANG[1,2]**, WENCHAO CHEN**[1,3]**, WEN-SHENG ZHAO**[4]**, (Senior Member, IEEE), GUO-DONG ZHU**[1]**, ZHEN-GUO ZHAO**[5]**, JOSÉ E. SCHUTT-AINÉ**[6]**, (Fellow, IEEE), AND WEN-YAN YIN**[1]**, (Fellow, IEEE)**

[1]Key Laboratory of Advanced Micro-Nano Electronic Devices and Smart Systems of Zhejiang Province, College of Information Science and Electronic Engineering, Innovative Institute of Electromagnetic Information and Electronic Integration, Zhejiang University, Hangzhou 310058, China
[2]State Key Laboratory of Modern Optical Instrumentation, Centre for Optical and EM Research, Zhejiang University, Hangzhou 310058, China
[3]ZJU-UIUC Institute, International Campus, Zhejiang University, Haining 314400, China
[4]School of Electronics and Information, Hangzhou Dianzi University, Hangzhou 310018, China
[5]Institute of Applied Physics and Computational Mathematics, Beijing 100088, China
[6]Electrical and Computer Engineering Department, University of Illinois at Urbana–Champaign, Urbana, IL 61801, USA

Corresponding authors: Wen-Sheng Zhao (wsh.zhao@gmail.com), Wenchao Chen (wenchaochen@zju.edu.cn), and Wen-Yan Yin (wyyin@zju.edu.cn)

ABSTRACT A hybrid finite volume–finite element method which can avoid overestimation of volume shared by each vertex in the meshing grid is proposed to solve the diffusive transport governed continuity equation. The simulation results demonstrate that the improved algorithm can eliminate unphysical distortions as compared to the conventional Scharfetter Gummel method. Based on the proposed algorithm, a parallel-computation simulator is developed for large-scale electrothermal simulation of resistive random access memory (RRAM) arrays, in which the domain decomposition method and J parallel adaptive unstructured mesh applications infrastructure are adopted. The validity, speedup, and scalability of the parallel simulator are investigated on the TianHe-2 supercomputer. Based on the simulated results, the electrothermal characteristics and reliability analysis of large-scale RRAM arrays are investigated in detail.

INDEX TERMS Domain decomposition method (DDM), drift diffusion, electrothermal modeling and simulation, finite element method (FEM), finite volume method (FVM), reliability, resistive random access memory (RRAM), thermal crosstalk.

I. INTRODUCTION

Physically, ion migration in resistive random access memory, carrier transport in conventional semiconductor devices, or other advection-diffusion transport phenomena can be described by the drift-diffusion equation [1], [2]. Owing to the advection-diffusion feature, strong nonlinearity, and mixed nature, the spatial discretization of the drift-diffusion equation is a crucial issue. Some early attempts have

The associate editor coordinating the review of this manuscript and approving it for publication was Baozhen Yao.

been made to discretize this equation using classical finite element method (FEM) and finite difference (FD) scheme [3]. However, critical mesh size, as well as huge computing source, is usually required in these methods. Particularly, divergence often takes place when they are used to solve advection-dominated problem. To handle this limitation, a series of discretization schemes such as quasi-Fermi FEM [2], [4], Scharfetter-Gummel (SG) method [5], [6], Streamline Upwinding Petrov Galerkin method (SUPG) [7], [8], Finite Box Integration SG (FBSG) method [8], and divergence free method [7]

IEEE *Access*

D.-W. Wang *et al.*: Improved Algorithm for Drift Diffusion Transport and Its Application on Large-Scale Parallel Simulation

have been proposed to discrete the drift-diffusion equation. Among them, the FBSG is the most popular adopted in commercial software, such as COMSOL, TCAD, and GSS [9], [10]. However, its accuracy and convergence highly depend on the quality of grid meshes, and it has inherent cross-winding effects for 2D and 3D problems due to the current density for integration fixed along the cell edges [3].

On the other hand, some modified methods such as the Petrov Galerkin FEM and parameter-free stabilized FEM have been proposed to solve 2D or 3D advection-diffusion problems [11]–[13]. Here, we develop a hybrid algorithm based on the finite volume-finite element (FVFEM) and SG methods. It allows to more effectively solve the drift-diffusion transport problem in electronic devices, including ion migration in RRAMs and diffusive carrier transport in semiconductor devices. The performance of the improved algorithm is examined and compared to previous algorithms.

In addition, a numerical scheme consisting of FVFEM-SG method and FEM is developed to analyze electrothermal coupling phenomena in large scale RRAM arrays, since self-heating becomes a significant issue as integration density increases and can lead to reliability problems, including performance degradation or even breakdown [14]–[16]. Inherently, the electrothermal processes are coupled together, making the simulation much more complicated, time-consuming, and often beyond the capability of a personal computer (PC). To the best of the authors' knowledge, no work has been done for the simulation of large scale RRAM array [17]–[20]. Hence, a high-performance parallel simulation strategy is urgently needed to help solve this large scale multiphysics problem. Benefiting from the development of domain decomposition method (DDM), the capability of modeling and simulation of large-scale problems has been upgraded significantly [22]–[24]. Here, the J parallel adaptive unstructured mesh applications infrastructure (JAUMIN) and DDM based double-level parallel scheme proposed in [25] is employed for multiphysics problem.

The paper is organized as follows. In Section II, an improved algorithm is introduced at first. Then, the physical model of RRAM, numerical discretization scheme and parallel approach are presented in Section III. In Section IV, the parallel simulator is evaluated and then utilized to study the electrothermal characteristics of RRAM arrays. Some conclusions are finally drawn in Section V.

II. ALGORITHM DEVELOPMENT
The continuity equation for diffusive transport process can be expressed as

$$\begin{cases} \nabla \cdot \vec{J} = \dfrac{\partial n}{\partial t} + R \\ n = n_d \mid_{\Gamma_D} \\ \vec{J} \cdot \vec{n} = h \mid_{\Gamma_n} \end{cases} \tag{1}$$

where n is the particle concentration which can be electron, hole in semiconductor, or oxygen vacancy in RRAM and so on, R is the recombination/generation

rate, n_d is the Dirichlet boundary condition, h is the Neumann boundary condition, and Γ_D and Γ_N represent the Dirichlet and Neumann boundary, respectively. The drift-diffusion current density $\vec{J}$ is given as

$$\vec{J} = \mu_n n \vec{E} + D_n \nabla n \tag{2}$$

where μ_n is the mobility, D_n is the diffusion coefficient, respectively, and $\vec{E}$ is the electric field intensity. In (2), $\mu_n n \vec{E}$ and $D_n \nabla n$ denote the drift and diffusion components, respectively.

When applying the FBSG to integrate the left-hand side of equation (1), the control volume shared by each vertex is determined by the circumcenter and center of each edge, as shown in Fig. 1(a). It is known that the circumcenter of an obtuse triangle lies outside the element, which results in an overestimation of the area shared by the vertex. In this context, it introduces unphysical disturbances to the algorithm that results in instability [3]. By contrast, the control volume for each vertex in the improved method is determined by the inner and edge centers, which guarantees that the volume is always inside the element, as shown in Fig. 1(b).
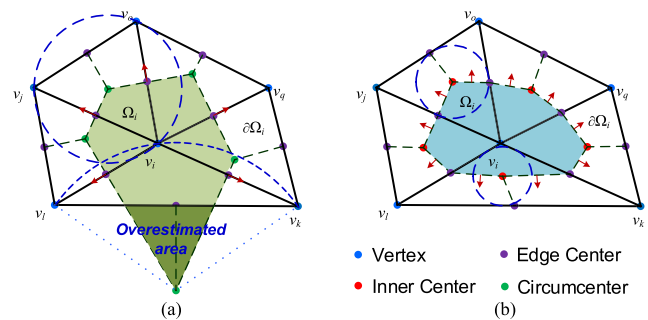
FIGURE 1. The control volume cell Ω_i around vertex v_i for triangle meshing grid in (a) FBSG and (b) the improved method which is named as FVFEM-SG.

Different from the FBSG, the outward normal current density of a finite volume cell Ω_i for the improved method must be treated carefully, since the current along each edge of a triangle element is no longer perpendicular to the outside surface of the volume cell Ω_i. As a remedy, Nedelec edge basis space is employed to extract the current density at midpoint of each segment in Ω_i by interpolation. The implementation of the improved method over control volume cell Ω_i are addressed below.

The governing equation (1) is integrated over the volume cell Ω_i

$$\frac{1}{q} \int_{\Omega_i} \nabla \cdot \vec{J} d\Omega = \int_{\Omega_i} \frac{\partial n}{\partial t} d\Omega + \int_{\Omega_i} R d\Omega \tag{3}$$

The Divergence theorem is applied to the left-hand side of (3) to obtain its 'weak' form, i.e.,

$$\frac{1}{q} \int_{\partial\Omega_i} \left(\vec{J} \cdot \vec{n} \right) dS = \int_{\Omega_i} \frac{\partial n}{\partial t} d\Omega + \int_{\Gamma_N} h dS + \int_{\Omega_i} R d\Omega \tag{4}$$

where $\partial\Omega_i$ is the boundary of Ω_i. By involving the standard Lagrangian basis $\{N\}$ [26], the particle density within each

D.-W. Wang *et al.*: Improved Algorithm for Drift Diffusion Transport and Its Application on Large-Scale Parallel Simulation

IEEE *Access*

mesh element can be expanded as

$$n = \sum_{m \in \Omega_{\text{tri}} \cup \Gamma_N} n_m N_m + \sum_{m \in \Gamma_D} n_{d,m}(t) N_m \quad (5)$$

where $m \in \Omega_{\text{tri}} \cup \Gamma_N$ denotes that the vertex v_m is in the interior of calculated domain or on the Neumann boundary, $m \in \Gamma_D$ denotes that the vertex v_m belongs to the Dirichlet boundary, and $n_{d,m}(t)$ is the time-dependent Dirichlet boundary value at the vertex v_m. As shown in Fig. 1(b), the control volume cell around the vertex v_i is composed of five parts belonging to five different mesh grids. To describe the problem more clearly, the integration over the part in mesh cell Δ_{ijo} will be elaborated in the following.

With the consideration of the upwind effect, the current density $\vec{J}$ described in (2) should be modified to SG formulation at each edge of the mesh cell. The SG formulation along the edge e_{ij} is expressed as

$$\left| \vec{J}_{ij} \right| = \frac{\mu_n E_{ij}}{2} \left(n_j \left[\coth \left(a_{ij} \right) + 1 \right] - n_i \left[\coth \left(a_{ij} \right) - 1 \right] \right) \quad (6)$$

where a_{ij} is the Reynolds number along the edge e_{ij}, and it can be calculated by $a_{ij} = \mu_n l_{ij} E_{ij} / (2D_n)$. l_{ij} is the length of edge e_{ij}, and E_{ij} is the electric field intensity along edge e_{ij}.

As mentioned above, the edge current is no longer perpendicular to the adjacent segment of boundary $\partial \Omega_i$ in the proposed FVFEM-SG. To get the outward norm, the Nedelec edge basis space is employed to interpolate the upwind edge current in (6) to the center of adjacent segment of boundary $\partial \Omega_i$ by [26]

$$\vec{J} = \sum_{e_{mp} \in E(\Delta_{ijo})} \left| \vec{J}_{pm} \right| \cdot \vec{W}_{pm} \quad (7)$$

By substituting (5)-(7) into (4), the integration over the area $\Delta_{ijo} \cap \Omega_i$ can be obtained as

$$\sum_{m \in \Delta_{ijo}} \frac{\partial n_m(t)}{\partial t} \int_{\Delta_{ijo} \cap \Omega_i} N_m d\Omega$$

$$- \sum_{e_{pm} \in E(\Delta_{ijo})} \frac{\mu_n E_{pm}}{2} \left(n_m \left[\coth \left(a_{pm} \right) + 1 \right] - n_p \left[\coth \left(a_{pm} \right) - 1 \right] \right)$$

$$\cdot \int_{\Delta_{ijo} \cap \partial \Omega i} \vec{W}_{pm} \cdot \vec{n} dS = - \int_{\Gamma N} h dS - \int_{\Delta ijo \cap} \Omega i R d\Omega \quad (8)$$

Although the second term in the left-hand side of (8) is over the edges, it operates on the node degree of freedoms. Therefore, (8) can be further simplified by rewriting the second term as double sum, i.e.,

$$\sum_{m \in \Delta_{ijo}} \frac{\partial n_m(t)}{\partial t} \int_{\Delta_{ijo} \cap \Omega_i} N_m d\Omega$$

$$- \sum_{m \in \Delta_{ijo}} n_m \sum_{e_{pm} \in E(\Delta_{ijo})} \sigma_{pm} \frac{\mu_n E_{pm}}{2} \left[\coth \left(a_{pm} \right) - \sigma_{pm} \right]$$

$$\cdot \int_{\Delta_{ijo}} \cap \partial \Omega i \vec{W}_{pm} \cdot \vec{n} dS = - \int_{\Gamma N} h dS - \int_{\Delta_{ijo}} \cap \Omega i R d\Omega \quad (9)$$

where $\sigma_{pm} = -1$ if e_{pm} is oriented from v_p to v_m, and $\sigma_{pm} = 1$ if e_{pm} is oriented in the opposite direction.

By calculating (9) at all vertices in the mesh cell Δ_{ijo}, the matrix form of (9) can be derived as

$$[M_e] \frac{\partial}{\partial t} \{n\} - [K_e] \{n\} = \{f_e\} \quad (10)$$

where K_e is the 'upwind' stiffness matrix and its element can be calculated by

$$K_{e,im} = \sum_{e_{pm} \in E(\Delta_{ijo})} \sigma_{pm} \frac{\mu_n E_{pm}}{2} \left[\coth \left(a_{pm} \right) - \sigma_{pm} \right]$$

$$\cdot \int_{\Delta_{ijo} \cap \partial \Omega_i} \vec{W}_{pm} \cdot \vec{n} \quad (11)$$

M_e is the damping matrix and its element can be calculated by

$$M_{e,im} = \int_{\Delta_{ijo} \cap \Omega_i} N_m \quad (12)$$

f_e is the column vector and its element can be calculated by

$$f_{e,i} = - \int_{\Gamma N} h dS - \int_{\Delta ijo \cap \Omega i} R d\Omega \quad (13)$$

Using the backward difference with respect to time, (10) can be discretized as

$$([M_e] - [K_e]) \{n\}_{t+\Delta t} = [M_e] \{n\}_t + \{f_e\} \quad (14)$$

where Δt is the time step for time evolution. The system equation for the problem domain can be obtained by summing (14) over all element as [26]

$$([M] - [K]) \{n\}_{t+\Delta t} = [M] \{n\}_t + \{f\} \quad (15)$$

where $[K]$ is the system 'upwind' stiffness matrix, and $[M]$ is the system damping matrix. This procedure can be easily extended to solve 3-D problems by replacing the control volume in Fig. 1(b) with the control volume composed of tetrahedron inner center, inner center of surface triangular, and center of edge in 3-D mesh cells. For steady-state case, the time-dependent term can be removed, i.e.,

$$- [K] \{n\} = \{f\} \quad (16)$$

The performance comparison between the improved method and conventional SG method will be given later.

III. MODELING AND SIMULATION SCHEMES
To verify the performance of our developed FVFEM-SG method, we apply it to a RRAM cell for algorithm evaluation, and further extend it to the large scale parallel simulation platform to solve multiphysics problems in RRAM arrays.

IEEE *Access*

D.-W. Wang *et al.*: Improved Algorithm for Drift Diffusion Transport and Its Application on Large-Scale Parallel Simulation

A. RRAM MODEL

RRAM is a promising candidate for future non-volatile memories due to its fast write/erase speed, large storage density, high efficiency and low power cost. The RRAM cell, shown in Fig. 2, stores information through high resistance state (HRS) and low resistance state (LRS) by rupture and formation of a conduction filament (CF) [27], [28]. HRS and LRS can be switched by an applied voltage.
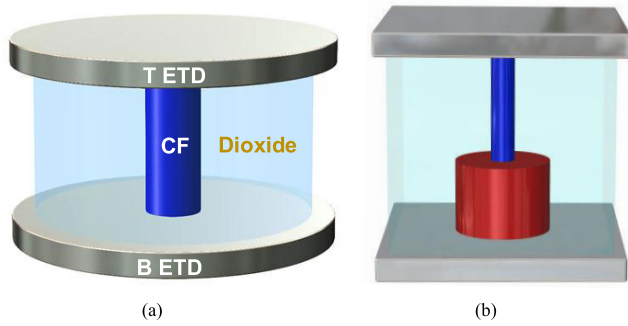
FIGURE 2. Schematics of (a) 1R RRAM cell and (b) 1D1R RRAM cell with cylindrical CF.

As mentioned above, the ion migration in a RRAM cell can be described by the drift-diffusion equation [18]. The transport of ions should satisfy the continuity equation:

$$\frac{1}{q} \nabla \cdot \vec{J} = \nabla \cdot \left(\mu\left(T\right) n_D \vec{E} + D\left(T\right) \nabla n_D \right) = \frac{\partial n_D}{\partial t} - R \tag{17}$$

where $\vec{E} = -\nabla V$, V is the voltage, and $\mu\left(T\right)$ and $D\left(T\right)$ are the temperature-dependent mobility and diffusion coefficient, respectively.

To get the electric field intensity, the current continuity equation needs to be solved,

$$\nabla \cdot \left(\sigma\left(n_D, T\right) \nabla V \right) = 0 \tag{18}$$

where $\sigma\left(n_D, T\right)$ is the electrical conductivity of the doped dioxide and n_D is particle concentration. $\sigma\left(n_D, T\right)$ can be given by Arrhenius equation:

$$\sigma\left(n_D, T\right) = \sigma_0 \exp\left(-\frac{E_{AC}}{k_B T} \right) \tag{19}$$

where σ_0 is the pre-exponential factor, E_{AC} is the activation energy for conduction, and k_B is the Boltzmann constant.

With increasing integration density, self-heating effect (SHE) becomes more and more significant in RRAM arrays which leads to a series of reliability issues, including performance degradation or even breakdown. To capture the temperature distribution due to self-heating, the thermal conduction equation should be solved, i.e.,

$$c\left(T\right) \frac{\partial T}{\partial t} = \kappa\left(n_D, T\right) \nabla^2 T + Q \tag{20}$$

where $c\left(T\right)$ is the temperature-dependent heat capacity, $Q = \vec{J} \cdot \vec{E}$ is the heat generation rate, and $\kappa\left(n_D, T\right)$ is the temperature- and particle concentration-dependent thermal conductivity. A nonlinear thermal conductivity model for HfO_x is specified as [18]

$$\kappa_{HfO} = \kappa_{HfO0} \left(1 + \lambda\left(T - T_0\right) \right) \tag{21}$$

where $\lambda = 0.01$ is the linear thermal coefficient. κ_{HfO0} is the thermal conductivity at $T_0 = 300K$, and it is a function of particle concentration as described in [18].

As seen from (17)–(20), the ion migration and thermal transport are coupled together through temperature- and particle concentration-dependent parameters.

B. NUMERICAL SCHEME

The flowchart for our proposed numerical algorithm is shown in Fig. 3. It can be seen that the nonlinear particle continuity equation is first solved self-consistently with the current continuity equation to determine the current and particle concentration distributions. From these, the heat generation rate is then calculated and set as an input for the thermal conduction equation. The updated temperature distribution is captured and coupled back to the current and particle concentration continuity equations through the temperature-dependent parameters. In this process, FEM is employed for discretizing the current continuity and thermal conduction equations, while FVFEM-SG method is used to solve the particle continuity equation. After the system matrix equations are obtained, they will be solved using an algebraic multigrid (AMG) solver.
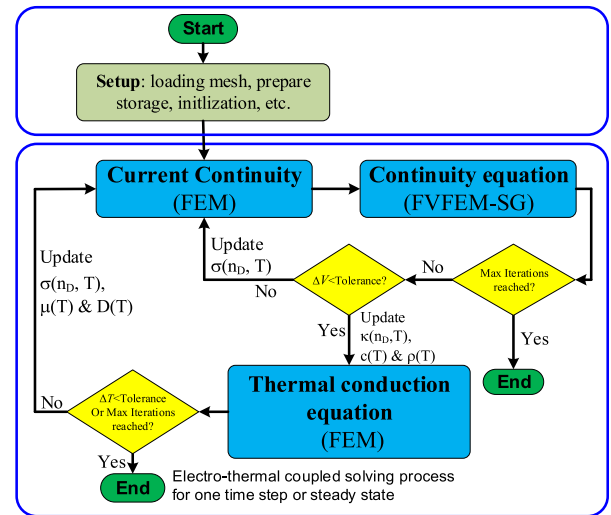
FIGURE 3. Flowchart of the proposed algorithm for electrothermal coupling problems in RRAM.

C. PARALLEL SIMULATION

Recently, electrothermal effects in RRAMs have been theoretically investigated [17], [18], using 2-D or small scale 3D array representations [19], [20]. As mentioned above, the electrothermal processes are coupled together, making the

D.-W. Wang *et al.*: Improved Algorithm for Drift Diffusion Transport and Its Application on Large-Scale Parallel Simulation

IEEE *Access*

simulation much more complicated, time-consuming, especially for large scale RRAM arrays. Consequently, a high-performance parallel multiphysics simulation is urgently required.
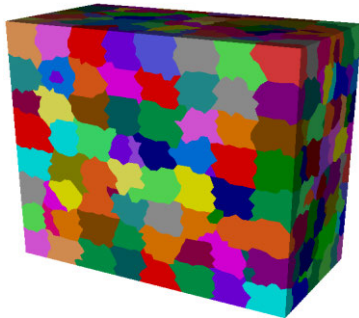

FIGURE 4. The generated patches for 512 CPU cores case.

In this context, a double level parallel scheme based on DDM and JAUMIN is employed [23], and simulations can be run on supercomputers with thousands of cores. After reading the mesh, as shown in Fig. 4, JAUMIN generates subdomains (called patches) using the METIS software package [29]. According to the inherent workload distribution scheme, these patches are distributed to every process. To balance the workload of parallel processes and dynamically minimize the number of successive patches assigned to each process, massage passing interface (MPI) parallel programming scheme is utilized. Then, the multi-process and multithread parallel strategy of the DDM is integrated into the JAUMIN framework. One processor generates a process to manage a series of patches and spawns several threads to the CPU cores of the processor. On each CPU core, the sublinear system is formed and then solved individually by AMG solver. In short, the double level parallel scheme improves the simulation process in the following three ways:

1) simulate the decomposed subdomains in parallel and independently to accelerate the computation;
2) exploit the deeper parallelization of the decomposed subsystems;
3) reduce the communication cost significantly among different computer nodes through balanced workload distribution.

Fig. 5 shows the hierarchical structure of the JAUMIN, which is organized into the supporting level, numerical level, and physical level. The supporting layer is composed of the implementation of parallelization, fundamental data structures, and adaptive algorithm. It can provide sufficient support to the other two levels. The physical level acts as a user interface to conduct the discretization of the physical model. The constructed matrices are transferred to the numerical level and then solved. More details of the JAUMIN can be found in [25].

IV. RESULTS AND DISCUSSION

The validity and parallel efficiency of the in-house developed simulator are examined in detail in this section. After that,
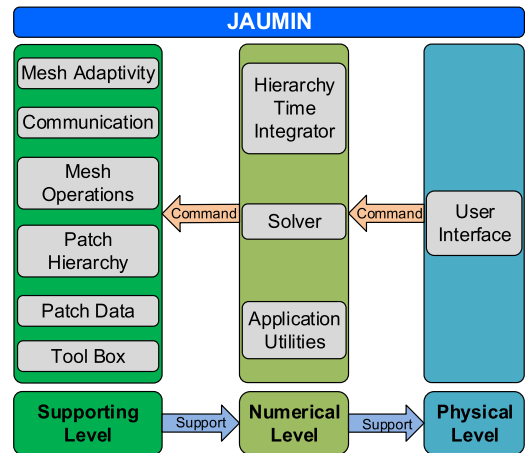

FIGURE 5. Hierarchical structure of the JAUMIN.

the simulator is utilized for the analysis of electrothermal characteristics of large scale RRAM arrays.

A. FVFEM-SG VS FBSG

As mentioned above, the FVFEM-SG method can overcome the shortcomings of the traditional SG strategy on requirements for meshing grid quality. To better understand this point, a 2-D example is first studied using these two methods on both high-quality and low-quality meshing grids as
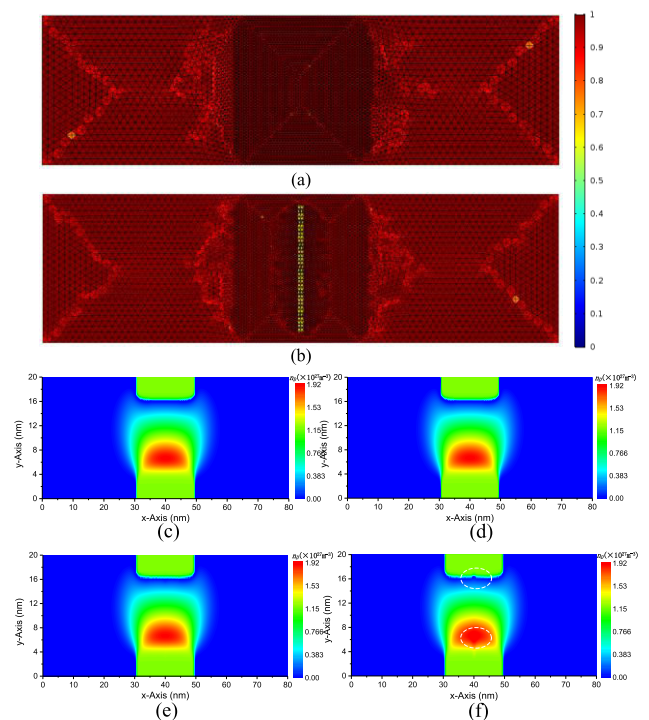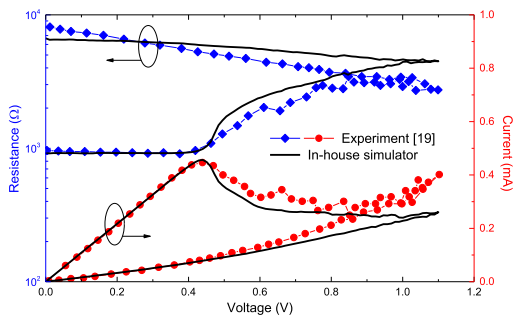

FIGURE 6. (a) and (b) Meshing grids for the same structure with different quality, the quality of meshing grid is measured from the color bar where higher value indicates higher quality; (c) and (d) give the particle distributions on high-quality mesh grid achieved by FVFEM-SG and FBSG methods respectively; (e) and (f) illustrate those on low quality mesh grid.

IEEE Access

D.-W. Wang *et al.*: Improved Algorithm for Drift Diffusion Transport and Its Application on Large-Scale Parallel Simulation

shown in Figs. 6(a) and (b). The simulated results are given in Figs. 6(c)-(f). It can be seen that both methods can achieve decent results for high-quality mesh grid while the FBSG results for low-quality mesh grid are distorted. Consequently, the FVFEM-SG method is deemed as a better choice for discretizing the RRAM like models.

B. ALGORITHM VALIDATION

The accuracy of our developed algorithm is validated through comparison with both experimental data [18] and commercial software. As shown in Fig. 2(a), one-resistor (1R) RRAMs with cylindrical CFs is taken as an example. According to [18], the CF is formed in the HfO$_2$ layer, which is sandwiched between the top and bottom electrode (ETD). The geometrical and physical parameters of the 1R RRAM cell are summarized in Table 1. The I-V and R-V curves of 1R cell in Fig. 7 are obtained by applying a triangular voltage sweep with ramp rate 1.1 V/s. It is evident that the simulated results using the in-house developed simulator agree well with the experimental data adopted from [18]. Further, the COMSOL Multiphysics is used to verify the accuracy of the in-house developed simulator by simulating a one-diode-one-resistor (1D1R) RRAM cell (see Fig. 2(b)). Table 2 gives the geometrical parameters of the 1D1R RRAM cell. As shown in Fig. 8, the results obtained by COMSOL Multiphysics and the in-house developed simulator are in good agreement with each other. The insets of Figs. 8(b) and 8(c) show the distributions of temperature and particle concentration along the CF.

TABLE 2. Geometrical parameters of the 1D1R RRAM cell.

Comp.	Materials	Geometrical parameters
B/W Line	Ni/Pt	$w_{etd} = 80$ nm $h_{etd} = 25$ nm
CF	HfO$_2$	$r_{CF} = 8$ nm $h_{CF} = 80$ nm
Cell Via Hole	HfO$_2$	$r_{CVH} = 80$ nm
Diode	Ti/TiO$_2$/Pt	$r_d = 40$ nm $h_d = 50$ nm

FIGURE 8. Comparison of simulation results between the in-house simulator and COMSOL in which a voltage source with ramp rate 1.1V/s is applied onto the top electrode. (a) Maximum temperature in the RRAM cell as a function of time, and the distributions of (b) temperature and (c) particle concentration along the cylindrical axis of the RRAM cell at 0.5 s.
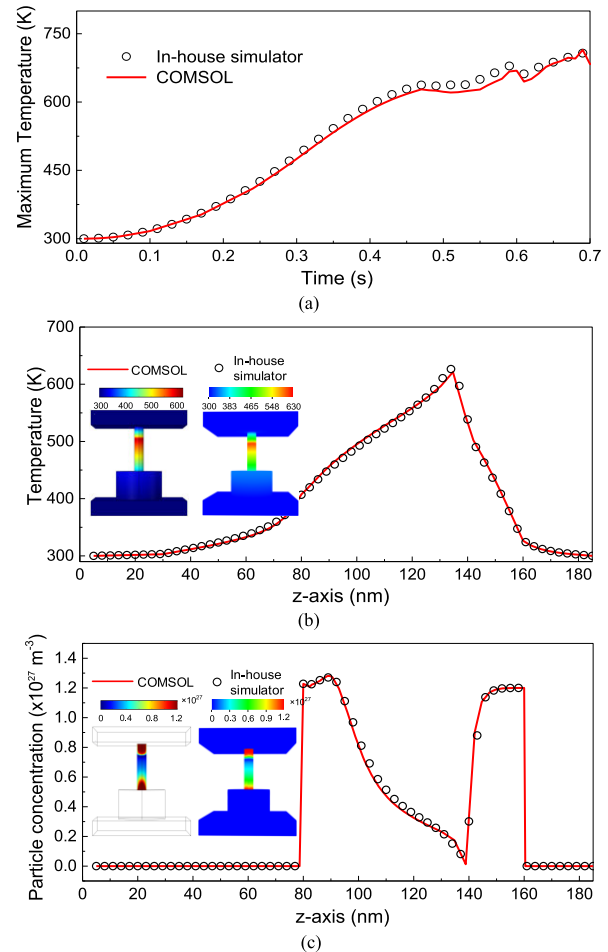

FIGURE 7. I-V and R-V characteristics of RRAM cell with CF diameter of 9 nm. The voltage was increased according to a triangular sweep with ramp rate 1.1 V/s.

TABLE 1. Geometrical and physical parameters of the 1R RRAM cell.

| Comp.	Materials	Geometrical parameters	Physical parameters
CF	HfO$_2$	$r_{CF} = 4.5$ nm $h_{CF} = 20$ nm	κ_{CF}: Eq. (21) $c_{CF} = 445$ J/kg°C σ_{CF}: Eq. (19)
Cell Via Hole	HfO$_2$	$r_{CVH} = 35$ nm $h_{CVH} = 20$ nm	$k_{CVH} = 0.5$ W/(m · K) $c_{CVH} = 445$ J/kg°C σ_{CVH}: Eq. (19)

C. SPEEDUP & SCALABILITY

Two indices, *speedup* and *scalability*, are typically used to evaluate the performance of parallel simulator [25]. The *speedup* which shows performance improvement in time cost with respect to problem size and core number, is defined as:

$$S = \frac{T(N_{core})}{T(M_{core})} \cdot \frac{Size(M_{core})}{Size(N_{core})} \quad (22)$$

D.-W. Wang *et al.*: Improved Algorithm for Drift Diffusion Transport and Its Application on Large-Scale Parallel Simulation

IEEE *Access*

where $T(\cdot)$ represents the Wall time (I/P/PDDM), $Size(\cdot)$ is the problem size which can be described by the degree of freedom. In (22), the case of N_{core} is taken as reference.

The *scalability* represents the scaling tendency of parallel algorithm with increasing number of cores or problem size.

$$\Phi = \frac{S}{M_{core}/N_{core}} \qquad (23)$$
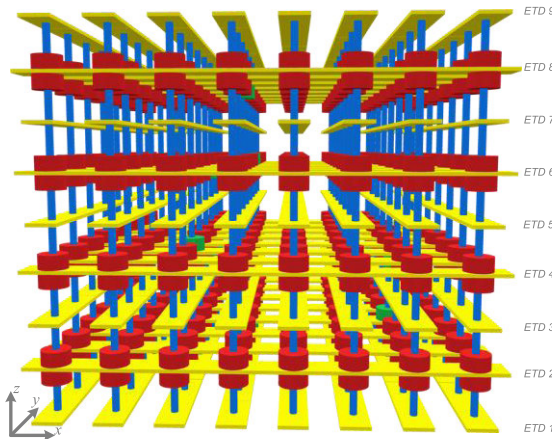
FIGURE 9. Schematic of the SBL cross-bar RRAM array with 512 cells (8 × 8 × 8). The golden strips represent the electrodes, blue cylinders are conduction filaments, and red and green cylinders represent the diodes at off and on states, respectively.

As shown in Fig. 9, a 512-cell (8 × 8 × 8) cross-bar RRAM array is taken as an example for parallel computing [27], [28]. The geometrical parameters of a one-diode-one-resistor (1D1R) RRAM cell are listed in Table 2. The cells in the array are randomly programmed, and the detailed power supply scheme is given in Table 3, where 0, 1, and −1 are the bias states for electrodes, representing dangling, high voltage and ground, respectively. A voltage sweep with ramp rate 1 V/s is applied to the biased electrode and the time step is chosen to be 0.01 s in the simulation.

TABLE 3. The states of each electrode in the RRAM array with 512 cells.

	s	s	s	s	s	s	s	s
ETD 1	0	0	1	0	0	0	0	0
ETD 2	0	0	−1	0	0	0	0	0
ETD 3	0	0	0	1	0	0	0	0
ETD 4	0	0	0	0	−1	0	0	0
ETD 5	0	0	1	0	0	0	0	0
ETD 6	0	0	−1	0	0	0	0	0
ETD 7	0	0	0	0	0	0	1	0
ETD 8	0	0	0	−1	0	0	0	0
ETD 9	0	0	0	1	0	0	0	0

Here, both the strong scalability and weak scalability of the in-house developed simulator are investigated. For the strong case, the degree of freedom is fixed at 47 470 182 and the simulated results are presented in Fig. 10(a) and Table 4. As given in Fig. 10(a), our algorithm can reach a *Speedup* of
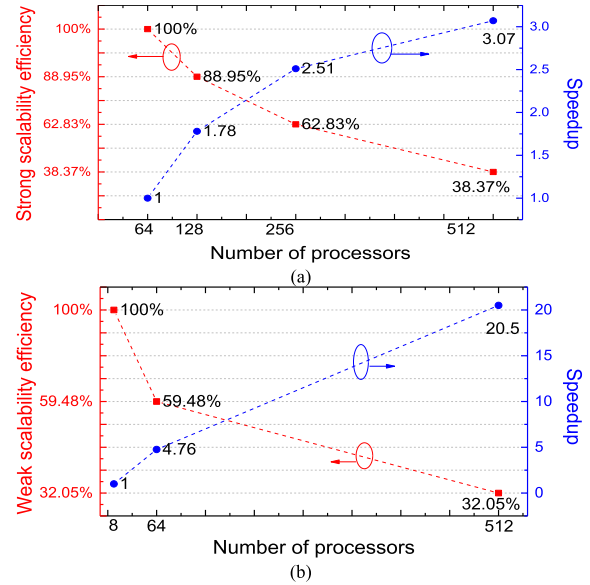
FIGURE 10. Scalability analysis on TianHe-II supercomputer. (a) Strong scalability and (b) weak scalability.

TABLE 4. Strong scalability experiment.

Number of DOFs (million)	Number of node/core/ process	Average CPU time per step (s)	Total nonlinear iterations	Total solver iterations
47.47	8/64/64	871.086	305	24589
	16/128/128	489.669	305	27830
	32/256/256	346.622	305	29332
	64/512/512	283.749	305	33135

3.07 and strong scalability efficiency of 38.37% on 512 CPU cores of 128 compute nodes, starting from 64 CPU cores of 16 compute nodes. Fig. 10(b) and Table 5 show the weak scalability results, in which 32.05% parallel efficiency is still achieved with a 64-fold increase in the problem size from 746 624 to 47 470 182, and computing resources from 8 CPU cores of 4 compute nodes to 512 CPU cores of 128 compute nodes. In Fig. 11 the simulated results of 47 470 182 size problem using 512 cores is given as an example. The drop in parallel efficiency with increasing problem size is mainly due to the following reasons:

1) For strong scalability, the time consumed by the AMG solver increases from 39.92% to 51.66% as the number of CPU cores increases from 64 to 512, implying that the solver will be less efficient when the size of the problem (matrix size) becomes smaller.

2) As given in Table 5, there are about 30% and 52% growth in the number of total solver iterations in the cases of 64 and 512 CPU cores compared with that of 8 CPU cores, respectively. As the patch number increases, the geometry size of each patch becomes smaller, thereby increasing the dependency between adjacent patches. In other word, more iterations are
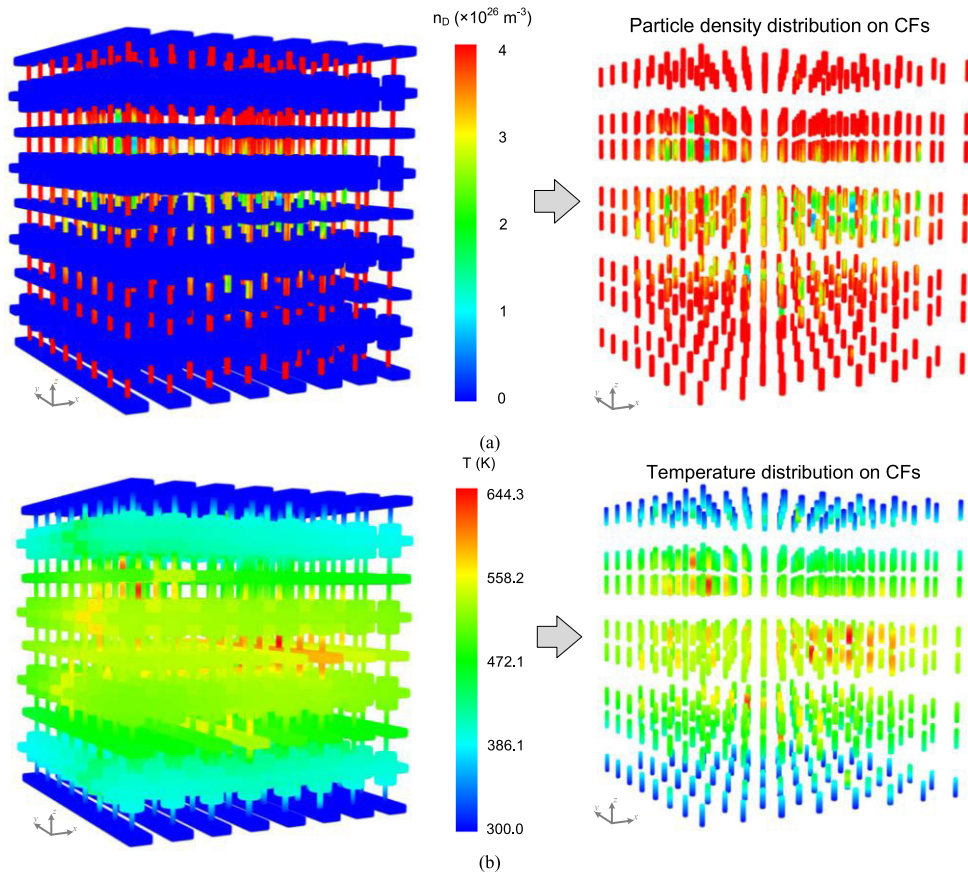
IEEE *Access*

D.-W. Wang *et al.*: Improved Algorithm for Drift Diffusion Transport and Its Application on Large-Scale Parallel Simulation

FIGURE 11. (a) Particle density and (b) temperature distributions in the 512-cell RRAM array at t=0.4s.

TABLE 5. Weak scalability experiment.

Number of DOFs (million)	Number of Node/Core/ Process	Average CPU time per step (s)	Total nonlinear iterations	Total solver iterations
0.75	1/8/8	85.241	296	21816
5.94	8/64/64	143.310	300	28302
47.47	64/512/512	283.749	305	33135

FIGURE 12. (a) Schematic of the SBL cross-bar RRAM array with 100 cells (5 × 5 × 4), in which four cells of the second layer marked in green are activated and (b) cross section of the second layer (k=2) of the RRAM array. Green and red represent the active and inactive cells, respectively.

required to achieve convergent global solution for one governing equation.

3) The increase in the number of patch and boundary increases the time consumed in the information exchange between the cores, thereby resulting in the decreased efficiency.

D. THERMAL CROSSTALK AND RELIABILITY ANALYSIS

In the highly integrated RRAM array, RRAM cell can be affected by adjacent cells, which degrades reliability or even may change its stored information. In this subsection, we carefully investigate the electrothermal effect in RRAM array, and the reliability problem induced by thermal crosstalk effect.
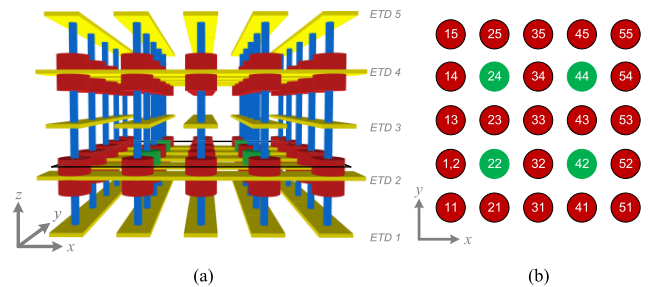
Fig. 12(a) shows a shared-bit-line (SBL) cross-bar RRAM array with 100 cells (5 × 5 × 4), each cell in RRAM array is with the same geometrical parameters as in Table 2. The cross section of the second layer (counted from the bottom) is depicted in Fig. 12(b). The cells in the array are denoted by $(ij)_k$, where i, j, and k represent the index number along the x-, y-, and z-directions, respectively. According to the power supply scheme in Table 6, four cells of the second layer are activated by injecting a rectangular pulse with amplitude of 1.2 V. All the other cells in the array are inactive.

D.-W. Wang *et al.*: Improved Algorithm for Drift Diffusion Transport and Its Application on Large-Scale Parallel Simulation

IEEE *Access*

TABLE 6. The bias states of electrodes in RRAM array with 100 cells.

	S	S	S	S	S
ETD 1	0	0	0	0	0
ETD 2	0	−1	0	−1	0
ETD 3	0	1	0	1	0
ETD 4	0	0	0	0	0
ETD 5	0	0	0	0	0
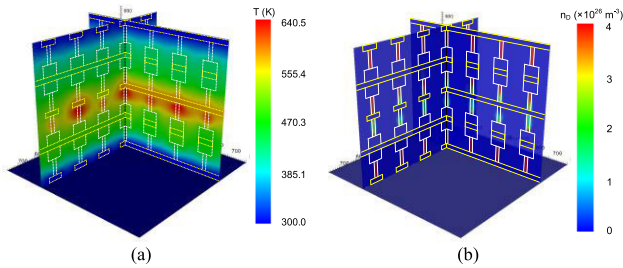
FIGURE 13. 3D (a) temperature and (b) particle density distribution of the SBL RRAM array sliced through the center of cells $(22)_k$ along both *x*- and *y*-directions.

FIGURE 14. (a) Temperature distribution, (b) particle density distribution, and (c) resistance ratio of the SBL RRAM array with 100 cells along the *z*-axis through centers of the cells $(22)_k$, $(23)_k$, $(32)_k$, and $(33)_k$.

Fig. 13 presents the simulated results in sliced planes through the center of cell $(22)_k$ along both x- and y-directions. To better understand the simulated results, temperature and particle density distribution along z-axis through certain cells are extracted and plotted in Figs. 13 (a) and (b), respectively. It is shown that three victim cells around the cell $(22)_2$, i.e., $(23)_2$, $(32)_2$, and $(33)_2$, are affected to various extents. The maximum temperatures of these victim cells reach 617.2 K at $z = 0.292\mu$m, 592.9 K at $z = 0.275\mu$m, and 533.6 K at $z = 0.306\mu$m, respectively. The cell $(33)_2$ exhibits the lowest crosstalk temperature among these victim cells, as it has a large distance to the active cells. Although the cells $(23)_2$ and $(32)_2$ have the same distance to the active cells, the cell $(23)_2$ suffers from larger crosstalk temperature due to the asymmetric structure of electrodes, which will be discussed in detail in the next paragraph. The resistance ratios (to the initial value) of the CFs of cells $(22)_k$, $(23)_k$, $(32)_k$, and $(33)_k$ are shown in Fig. 14(c). It can be seen that the resistance ratio of the victim cell $(23)_2$ can reach greater than 2, which may cause loss of the stored information [18].

To explain the related in detail, an equivalent thermal resistance networks are established as in Fig. 15. The thermal conductivity of HfOx is expressed as $\kappa_{HfO} = a \cdot n_D + b$, where $a = 1.875 \times 10^{-26}$W $\cdot$ m^2/K, $b = 0.5$W/m $\cdot$ K and n_D is the particle density (in m^{-3}). Here, the background density n_D in HfOx is set to be 1×10^{22}m^{-3}, and κ_{HfO} is calculated as 0.5W/m $\cdot$ K, which is much smaller than that of the metal electrode. Hence, the metal electrode has much low thermal resistance compared to HfOx. Heat dissipates more effectively in thermal resistance network (a) than (b). Therefore, the cell $(23)_2$ suffers from severer thermal crosstalk than the cell $(32)_2$, which is consistent with the results in Fig. 14(a).
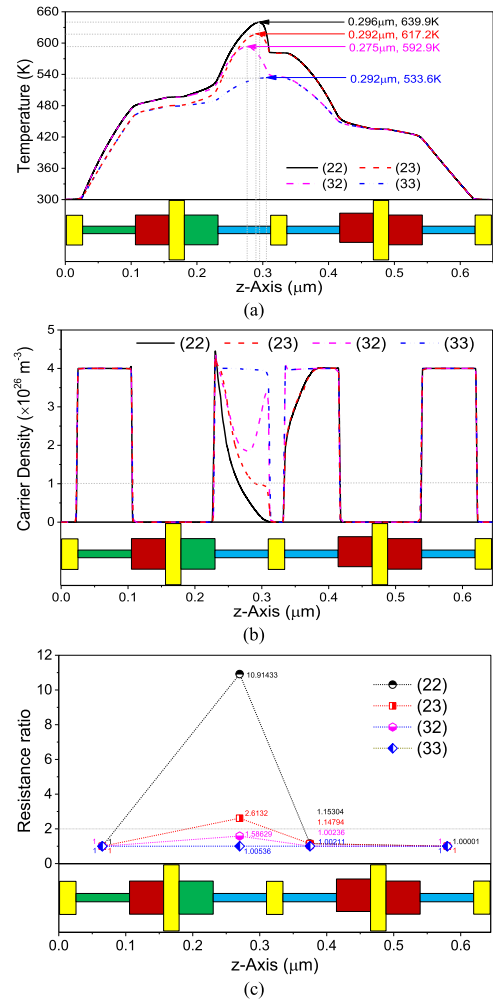
The effects of various structural parameters, including the radius of cylindrical CF, and the cell size, on the thermal crosstalk in the victim cell $(23)_2$ are further studied.

1) RADIUS

Fig. 16 shows the temperature distribution of the RRAM array along the *z*-direction through the center of victim cell $(23)_k$. As the radius of CF increases from 6 nm to 10 nm, the maximum crosstalk temperature increases from 580.2K to 650.6 K. This is due to the fact that decreasing the radius increases the CF resistance, thereby suppressing the power consumption and SHE in the RRAM array. Fig. 17 shows the 3D temperature distributions of the CRRAM arrays for different r_{cf}. However, the decrease in the power will degrade the switching performance of the RRAM cells, which is reflected by the variation of the resistance ratio (see Fig. 18).

It can be seen from Fig. 18 that the thermal crosstalk has a negligible influence on the resistance ratio of victim cell $(23)_2$ as $r_{cf} = 6$nm, and it becomes more significant as
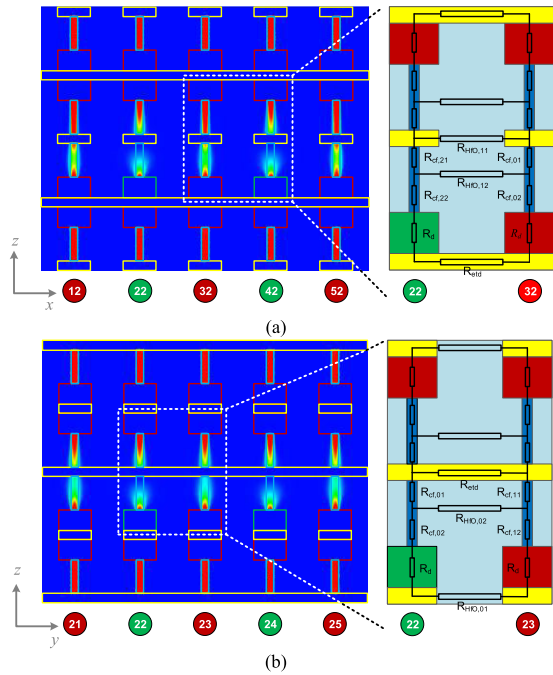
FIGURE 15. Particle density distribution sliced through the center of cell (22) along the (a) *x*- and (b) *y*-directions and the corresponding thermal resistance networks.
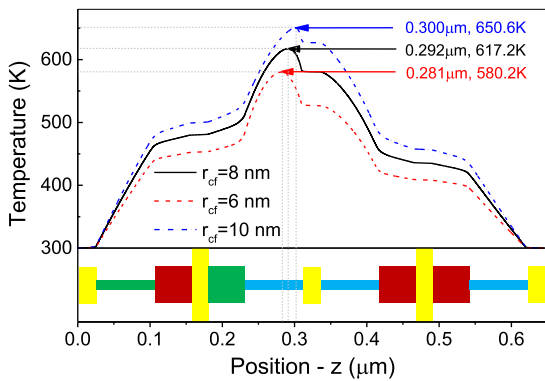

FIGURE 16. Steady-state temperature distribution of the RRAM array along the *z*-direction through the center of cell $(23)_k$ with different r_{cf}.
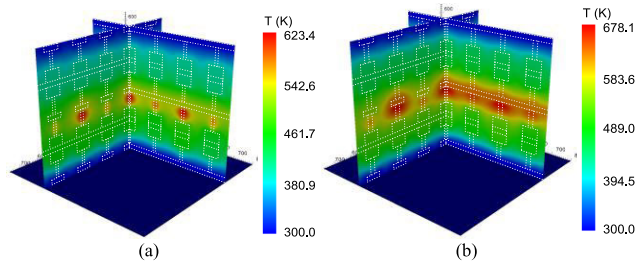

FIGURE 17. 3D temperature distribution of the RRAM array sliced through the center of (22) along both *x*- and *y*-directions with (a) r_{cf} = 6nm and (b) r_{cf} = 10nm.

r_{cf} increases, which is similar to the variation tendency of the crosstalk temperature shown in Fig. 16. As explained earlier, the larger the CF radius, the higher the power consumption,
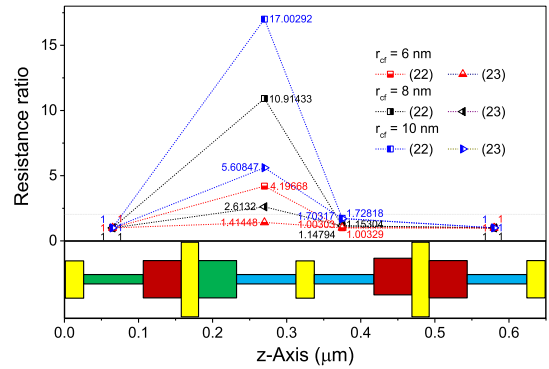

FIGURE 18. Resistance ratio of the cells $(22)_k$ and $(23)_k$ with different r_{cf} in the RRAM array.

and consequently, the sharper the temperature rise in the programmed cell. This phenomenon is also reflected by the variation of the resistance ratio of the cell $(22)_2$, as shown in Fig. 18. Furthermore, the 3D particle density distribution of the RRAM arrays with r_{cf} of 6 nm and 10 nm are plotted in Fig. 19.
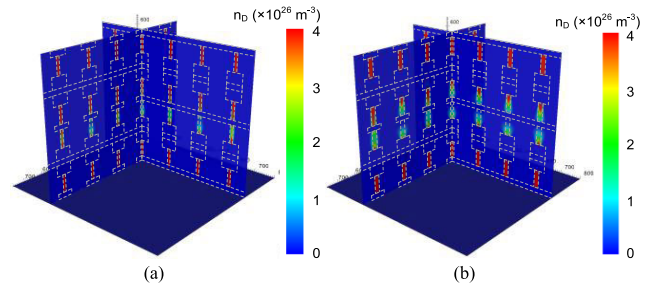

FIGURE 19. 3D particle density distribution of the RRAM array sliced through the center of cell (22) along both x- and y-directions with (a) r_{cf} = 6nm and (b) r_{cf} = 10nm.

2) CELL SIZE

The effects of cell size on the thermal crosstalk are investigated. Fig. 20 shows the temperature along the *z*-direction through the center of victim cell $(23)_k$. As p_{cell} increase
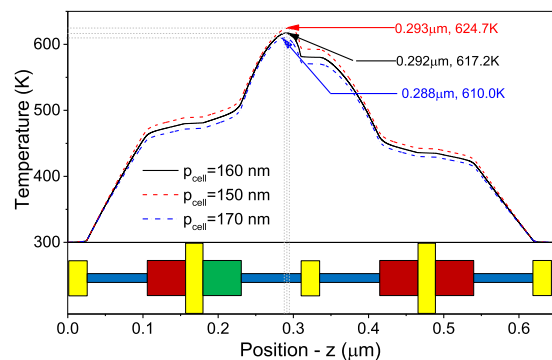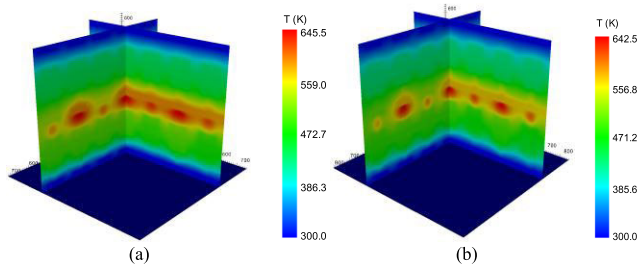

FIGURE 20. Temperature distribution of the RRAM array along the *z*-direction through the center of cell $(23)_k$ with different p_{cell}.

D.-W. Wang *et al.*: Improved Algorithm for Drift Diffusion Transport and Its Application on Large-Scale Parallel Simulation

IEEE Access

FIGURE 21. 3D temperature distribution of the RRAM array sliced through the center of the cells $(24)_k$ along both *x*- and *y*-directions with (a) p_{cell} = 150nm, and (b) p_{cell} = 170nm.

FIGURE 22. Resistance ratio of the cells $(22)_k$ and $(23)_k$ in the RRAM array with different p_{cell}

FIGURE 23. 3D particle density distribution of the RRAM array sliced through the center of cell $(22)_k$ along the *x*- and *y*-direction with (a) p_{cell} = 150nm, and (b) p_{cell} = 170nm.

from 150 nm to 170 nm, the maximum crosstalk temperature decreases slightly from 624.7 K to 610 K, which is due to the decrease of power density. Fig. 21 shows the 3D temperature distribution of the RRAM arrays with different p_{cell}.

The resistance ratio of the cells $(22)_k$ and $(23)_k$ with different p_{cell} are shown in Fig. 22. It can be seen that as p_{cell} increases from 150 to 170 nm, the resistance ratio of the cell $(23)_2$ decreases from 3.42 to 2.41 due to the decrease of temperature. The 3D particle density distribution of the RRAM arrays with p_{cell} of 150 nm and 170 nm are plotted in Fig. 23.
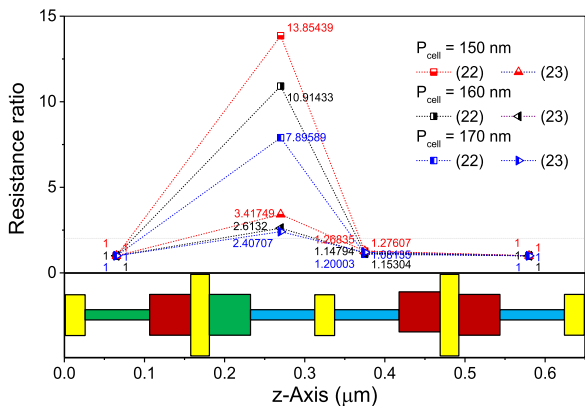
V. CONCLUSION

In this paper, FVFEM-SG method is developed for solving the continuity equation for diffusive transport in electronic devices. The algorithm stability is improved over the traditional FBSG method, especially in the condition of low meshing quality. A high performance parallel-computation simulator based on the domain decomposition method and J parallel adaptive unstructured mesh applications infrastructure is developed for large scale electrothermal simulation of resistive random access memory (RRAM) arrays, in which the FVFEM-SG is used to solve the ion migration process. *Speedup* and *scalability* of the parallel algorithm up to 512 computer cores are investigated on supercomputer TianHe-2. The effects of various structural parameters, including conductive filament (CF) radius, and cell size, on the electrothermal characteristics of RRAM arrays are captured and studied.
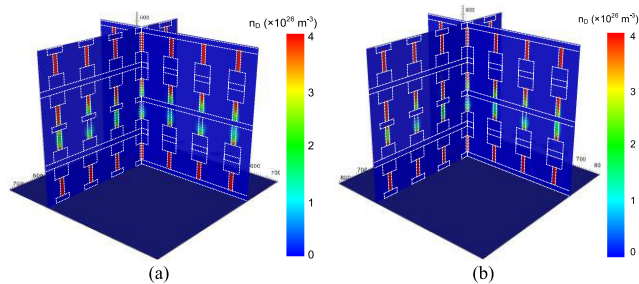
VI. ACKNOWLEDGEMENT

REFERENCES

[1] S. Asapu and T. Maiti, "Multifilamentary conduction modeling in transition metal oxide-based RRAM," *IEEE Trans. Electron Devices*, vol. 64, no. 8, pp. 3145–3150, Aug. 2017. doi: 10.1109/TED.2017.2709249.

[2] E. Patrick, N. Rowsey, and M. E. Law, "Total Dose radiation damage: A simulation framework," *IEEE Trans. Nucl. Sci.*, vol. 62, no. 4, pp. 1650–1657, Aug. 2015. doi: 10.1109/TNS.2015.2425226.

[3] G. Ghione and A. Benvenuti, "Discretization schemes for high-frequency semiconductor device models," *IEEE Trans. Antennas Propag.*, vol. 45, no. 3, pp. 443–456, Mar. 1997. doi: 10.1109/8.558659.

[4] M. N. Tutt and C. C. Mcandrew, "Physical and numerically stable Linvill-lump compact model of the pn-junction," *IEEE J. Electron Devices Soc.*, vol. 4, no. 2, pp. 90–98, Mar. 2016. doi: 10.1109/JEDS.2016.2517190.

[5] D. L. Scharfetter and H. K. Gummel, "Large-signal analysis of a silicon Read diode oscillator," *IEEE Trans. Electron Devices*, vol. ED-16, no. 1, pp. 64–67, Jan. 1969. doi: 10.1109/T-ED.1969.16566.

[6] H. Siemund and H. Göbel, "Numerical simulation of organic light-emitting diodes with insulating cathode buffer layer," *IEEE Trans. Electron Devices*, vol. 63, no. 9, pp. 3700–3706, Sep. 2016. doi: 10.1109/TED.2016.2593714.

[7] R. E. Bank, J. F. Bürgler, W. Fichtner, and R. K. Smith, "Some upwinding techniques for finite element approximations of convection-diffusion equations," *Numerische Mathematik*, vol. 58, no. 1, pp. 185–202, Dec. 1990. doi: 10.1007/BF01385618.

[8] A. Mauri, A. Bortolossi, G. Novielli, and S. Riccardo, "3D finite element modeling and simulation of industrial semiconductor devices including impact ionization," *J. Math. Ind.*, vol. 5, no. 1, pp. 1–18, 2015. doi: 10.1186/s13362-015-0015-z.

[9] *ATLAS User's Manual: Device Simulation Software*, Silvaco International, Santa Clara, CA, USA, 2016.

[10] *COMSOL Multiphysics Semiconductor Module User's Guide*, COMSOL AB, Burlington, MA, USA, 2012.

[11] P. Bochev, K. Peterson, and X. Gao, "A new control volume finite element method for the stable and accurate solution of the drift–diffusion equations on general unstructured grids," *Comput. Methods Appl. Mech. Eng.*, vol. 254, pp. 126–145, Feb. 2013. doi: 10.1016/j.cma.2012.10.009.

[12] Y. Lian, Y. Ying, S. Tang, S. Lin, G. J. Wagner, and W. K. Liu, "A Petrov–Galerkin finite element method for the fractional advection–diffusion equation," *Comput. Methods Appl. Mech. Eng.*, vol. 309, pp. 388–410, Jun. 2016. doi: 10.1016/j.cma.2016.06.013.

[13] P. Bochev and K. Peterson, "A parameter-free stabilized finite element method for scalar advection-diffusion problems," *Central Eur. J. Math.*, vol. 11, no. 8, pp. 1458–1477, 2013. doi: 10.2478/s11533-013-0250-8.

IEEE *Access*

D.-W. Wang *et al.*: Improved Algorithm for Drift Diffusion Transport and Its Application on Large-Scale Parallel Simulation

[14] F. García-Redondo, P. Royer, M. López-Vallejo, H. Aparicio, P. Ituero, and C. A. López-Barrio, "Reconfigurable writing architecture for reliable RRAM operation in wide temperature ranges," *IEEE Trans. Very Large Scale Integr. (VLSI) Syst.*, vol. 25, no. 4, pp. 1224–1235, Apr. 2017. doi: 10.1109/TVLSI.2016.2634083.

[15] P. Sun *et al.*, "Thermal crosstalk in 3-dimensional RRAM crossbar array," *Sci. Rep.*, vol. 5, Aug. 2015, Art. no. 13504. doi: 10.1038/srep13504.

[16] X. H. Wang, H. Wu, B. Gao, X. Li, N. Deng, and H. Qian, "Thermal stability of HfO$_x$-based resistive memory array: A temperature coefficient study," *IEEE Electron Device Lett.*, vol. 39, no. 2, pp. 192–195, Feb. 2018. doi: 10.1109/LED.2017.2787124.

[17] S. Kim *et al.*, "Physical electro-thermal model of resistive switching in bi-layered resistance-change memory," *Sci. Rep.*, vol. 3, Apr. 2013, Art. no. 1680. doi: 10.1038/srep01680.

[18] S. Larentis, F. Nardi, S. Balatti, D. C. Gilmer, and D. Ielmini, "Resistive switching by voltage-driven ion migration in bipolar RRAM—Part II: Modeling," *IEEE Trans. Electron Devices*, vol. 59, no. 9, pp. 2468–2475, Sep. 2012. doi: 10.1109/TED.2012.2202320.

[19] Y. Luo, W. Chen, M. Cheng, and W.-Y. Yin, "Electrothermal characterization in 3-D resistive random access memory arrays," *IEEE Trans. Electron Devices*, vol. 6, no. 12, pp. 4720–4728, Dec. 2016. doi: 10.1109/IMWS-AMP.2016.7588366.

[20] S. Li *et al.*, "Fully coupled multiphysics simulation of crosstalk effect in bipolar resistive random access memory," *IEEE Trans. Electron Devices*, vol. 64, no. 9, pp. 3647–3653, Sep. 2017. doi: 10.1109/TED.2017.2730857.

[21] S.-C. Lee, M. N. Vouvakis, and J.-F. Lee, "A non-overlapping domain decomposition method with non-matching grids for modeling large finite antenna arrays," *J. Comput. Phys.*, vol. 203, no. 1, pp. 1–21, Feb. 2005. doi: 10.1016/j.jcp.2004.08.004.

[22] Z. Peng and J.-F. Lee, "Non-conformal domain decomposition method with second-order transmission conditions for time-harmonic electromagnetics," *J. Comput. Phys.*, vol. 229, no. 16, pp. 5615–5629, Aug. 2010. doi: 10.1016/j.jcp.2010.03.049.

[23] Q. Liu, W. Zhao, J. Cheng, Z. Mo, A. Zhang, and J. Liu, "A programming framework for large scale numerical simulations on unstructured mesh," in *Proc. IEEE 2nd Int. Conf. Big Data Secur. Cloud*, Apr. 2016, pp. 310–315. doi: 10.1109/BigDataSecurity-HPSC-IDS.2016.12.

[24] P. Aristidou, D. Fabozzi, and T. Van Cutsem, "Dynamic simulation of large-scale power systems using a parallel Schur-complement-based decomposition method," *IEEE Trans. Parallel Distrib. Syst.*, vol. 25, no. 10, pp. 2561–2570, Oct. 2014. doi: 10.1109/TPDS.2013.252.

[25] W.-J. Wang *et al.*, "Massively parallel simulation of large-scale electromagnetic problems using one high-performance computing scheme and domain decomposition method," *IEEE Trans. Electromagn. Compat.*, vol. 59, no. 5, pp. 1523–1531, Oct. 2017. doi: 10.1109/TEMC.2017.2656891.

[26] J.-M. Jin, *The Finite Element Method in Electromagnetics*, 3nd ed. New York, NY, USA: Wiley, 2014.

[27] T.-C. Chang, K.-C. Chang, T.-M. Tsai, T.-J. Chu, and S. M. Sze, "Resistance random access memory," *Mater. Today*, vol. 19, no. 5, pp. 254–264, Jun. 2016. doi: 10.1016/j.mattod.2015.11.009.

[28] H.-S. P. Wong *et al.*, "Metal–Oxide RRAM," *Proc. IEEE*, vol. 100, no. 6, pp. 1951–1970, Jun. 2012. doi: 10.1109/JPROC.2012.2190369.

[29] S. U. Ansari *et al.*, "Mesh partitioning and efficient equation solving techniques by distributed finite element methods: A survey," *Arch. Comput. Methods Eng.*, vol. 26, no. 1, pp. 1–16, Jan. 2019. doi: 10.1007/s11831-017-9227-2.

[30] J. Y. Seok *et al.*, "A review of three-dimensional resistive switching crossbar array memories from the integration and materials property points of view," *Adv. Funct. Mater.*, vol. 24, no. 34, pp. 5316–5339, Jul. 2014. doi: 10.1002/adfm.201303520.

WENCHAO CHEN received the B.E. degree in information engineering from Xi'an Jiaotong University, Xi'an, China, in 2006, the M.E. degree in electronic engineering from Shanghai Jiao Tong University, Shanghai, China, in 2009, and the Ph.D. degree in electrical and computer engineering from the University of Florida, Gainesville, FL, USA, in 2014.

He is currently an Assistant Professor with the ZJU-UIUC Institute, Zhejiang University, Haining, China. His research interests include multiphysics modeling and simulation of emerging electronic devices, and 3D ICs.

WEN-SHENG ZHAO (S'09–M'13–SM'18) received the B.E. degree from the Harbin Institute of Technology, Harbin, China, in 2008, and the Ph.D. degree from Zhejiang University, Hangzhou, China, in 2013.

He was a Visiting Ph.D. Student with the National University of Singapore, Singapore, from 2010 to 2013, and a Visiting Scholar with the Georgia Institute of Technology, Atlanta, GA, USA, from 2017 to 2018. He is currently an Associate Professor with Hangzhou Dianzi University, Hangzhou. He has published one book, three book chapters, and over 50 international journal articles (more than 30 IEEE papers). His research interests include signal integrity and EMC, carbon nanoelectronics, multiphysics simulation, microwave sensors, and machine learning applications in electronic design.

GUO-DONG ZHU received the B.S. degree in electronic engineering from the University of Electronic Science and Technology of China, Chengdu, China, in 2015. He is currently pursuing the M.S. degree in optical engineering with Zhejiang University, Hangzhou, China.

His current research interests include multiphysics modeling and simulation with a focus on resistive switching memories, integrated circuits, and parallel computing.

DA-WEI WANG received the B.E. degree in communication engineering from Jilin University, Changchun, China, in 2010, and the M.E. degree in communication and information system from the China Academy of Telecommunication Technology, Beijing, China, in 2013. He is currently pursuing the Ph.D. degree in electronic science and technology with Zhejiang University, Hangzhou, China. His current research interests include computational electromagnetics, signal integrity analysis, and multiphysics simulation.

ZHEN-GUO ZHAO received the B.S. degree in microelectronic from Shandong University, Jinan, China, in 2010, and the M.S. degree in radio physics from the Graduate School, China Academy of Engineering Physics, Beijing, China, in 2013.

He is currently with the Institute of Applied Physics and Computational Mathematics, Beijing. His research interests include device physics and numerical simulation, parallel numerical methods in multiphysics, and effects of high-power electromagnetic pulse.

D.-W. Wang *et al.*: Improved Algorithm for Drift Diffusion Transport and Its Application on Large-Scale Parallel Simulation

IEEE *Access*

JOSÉ E. SCHUTT-AINÉ (S'86–M'86–SM'98–F'07) received the B.S. degree in electrical engineering from the Massachusetts Institute of Technology, Cambridge, MA, USA, in 1981, and the M.S. and Ph.D. degrees from the University of Illinois at Urbana–Champaign (UIUC), Urbana, IL, USA, in 1984 and 1988, respectively.

From 1981 to 1983, he was with the Hewlett Packard Technology Center, Santa Rosa, CA, USA, as an Application Engineer, where he was involved in research on microwave transistors and high-frequency circuits. In 1988, he joined the Electrical and Computer Engineering Department, UIUC, as a member of Electromagnetics and Coordinated Science Laboratories, where he is currently involved in research on signal integrity for high-speed digital and high-frequency applications. He is a consultant for several corporations. His current research interests include the study of signal integrity and the generation of computer-aided design tools for high-speed digital systems.

Dr. Schutt-Ainé was a recipient of several research awards, including the 1991 National Science Foundation (NSF) MRI Award, the NASA Faculty Award for Research, in 1992, the NSF MCAA Award, in 1996, and the UIUC-NCSA Faculty Fellow Award, in 2000. He has also received several publication awards, including the IEEE Electrical Design of Advanced Packaging and Systems Symposium-2013 Best Paper Award and the IEEE Electrical Performance of Electronic Packaging-2014 Best Paper Award. He is currently serving as the Co-Editor-in-Chief of the IEEE Transactions on Components, Packaging and Manufacturing Technology.

WEN-YAN YIN (M'99–SM'01–F'13) received the M.Sc. degree in electromagnetic field and microwave technique from Xidian University, Xi'an, China, in 1989, and the Ph.D. degree in electrical engineering from Xi'an Jiaotong University, Xi'an, in 1994.

He was an Associate Professor with the Department of Electronic Engineering, Northwestern Polytechnic University, Xi'an, from 1993 to 1996. From 1996 to 1998, he was a Research Fellow with the Department of Electrical Engineering, Duisburg University, Duisburg, Germany. Since 1998, he has been with the Monolithic Microwave Integrated Circuit Modeling and Package Laboratory, Department of Electrical Engineering, National University of Singapore (NUS), Singapore, as a Research Fellow. In 2002, he joined Temasek Laboratories, NUS, as a Research Scientist and the Project Leader of High-Power Microwave and Ultrawideband Electromagnetic Compatibility (EMC)/Electromagnetic Interference. Since 2005, he has been a Professor of electromagnetic fields and microwave techniques with the School of Electronic Information and Electrical Engineering, Shanghai Jiao Tong University, Shanghai, China, where he is currently the Director and the Adjunct Ph.D. Candidate Supervisor with the Center for Microwave and RF Technologies. In 2009, he joined the Centre for Optical and Electromagnetic Research, National State Key Laboratory of Modern Optical Instrumentation, Zhejiang University, Hangzhou, China, as a *Qiu Shi* Chair Professor. As the Lead Author, he has authored over 270 international journal articles (more than 100 IEEE papers), including one international book and 17 book chapters. His current research interests include passive and active RF and millimeter-wave device and circuit modeling, ultrawideband interconnects and signal integrity, nanoelectronics, EMC and electromagnetic protection of communication platforms, and computational multiphysics and its application.

Dr. Yin received the Science and Technology Promotion Award of the First Class from the Local Shanghai Government of China, in 2005, the National Technology Invention Award of the Second Class from the Chinese Government, in 2008, the National Technology Progress Award of the Second Class from the Chinese Government, in 2012, and the best paper awards from the Asia-Pacific Symposium on Electromagnetic Compatibility, in 2008 and 2012, respectively. He was an IEEE EMC Society Distinguished Lecturer, from 2011 to 2012, and the General Co-Chair of the IEEE Electrical Design of Advanced Packaging and Systems Symposium (EDAPS), in 2011 and 2017, technically sponsored by the IEEE Components, Packaging and Manufacturing Technology Committee. He was also the Technical Chair of EDAPS, in 2006. He has been an Associate Editor of the IEEE Transactions on Components, Packaging and Manufacturing Technology and the IEEE Journal of Multiscale and Multiphysics Computational Techniques, since 2011. He was an Associate Editor of the *International Journal of Numerical Modeling: Electronic Networks, Devices and Fields*, from 2011 to 2016. He was a Guest Editor of the special issue on the IEEE Transactions on Electromagnetic Compatibility. He is a Reviewer of many international journals, including eight IEEE Transactions and IEEE letters.

● ● ●